NASA/TM—2001-210461

Structural Analysis of Composite Flywheels: An Integrated NDE and FEM Approach

Ali Abdul-Aziz, George Baaklini, and Jeffrey Trudell
Glenn Research Center, Cleveland, Ohio

January 2001

The NASA STI Program Office . . . in Profile

Since its founding, NASA has been dedicated to the advancement of aeronautics and space science. The NASA Scientific and Technical Information (STI) Program Office plays a key part in helping NASA maintain this important role.

The NASA STI Program Office is operated by Langley Research Center, the Lead Center for NASA's scientific and technical information. The NASA STI Program Office provides access to the NASA STI Database, the largest collection of aeronautical and space science STI in the world. The Program Office is also NASA's institutional mechanism for disseminating the results of its research and development activities. These results are published by NASA in the NASA STI Report Series, which includes the following report types:

- TECHNICAL PUBLICATION. Reports of completed research or a major significant phase of research that present the results of NASA programs and include extensive data or theoretical analysis. Includes compilations of significant scientific and technical data and information deemed to be of continuing reference value. NASA's counterpart of peer-reviewed formal professional papers but has less stringent limitations on manuscript length and extent of graphic presentations.

- TECHNICAL MEMORANDUM. Scientific and technical findings that are preliminary or of specialized interest, e.g., quick release reports, working papers, and bibliographies that contain minimal annotation. Does not contain extensive analysis.

- CONTRACTOR REPORT. Scientific and technical findings by NASA-sponsored contractors and grantees.

- CONFERENCE PUBLICATION. Collected papers from scientific and technical conferences, symposia, seminars, or other meetings sponsored or cosponsored by NASA.

- SPECIAL PUBLICATION. Scientific, technical, or historical information from NASA programs, projects, and missions, often concerned with subjects having substantial public interest.

- TECHNICAL TRANSLATION. English-language translations of foreign scientific and technical material pertinent to NASA's mission.

Specialized services that complement the STI Program Office's diverse offerings include creating custom thesauri, building customized data bases, organizing and publishing research results . . . even providing videos.

For more information about the NASA STI Program Office, see the following:

- Access the NASA STI Program Home Page at ***http://www.sti.nasa.gov***

- E-mail your question via the Internet to help@sti.nasa.gov

- Fax your question to the NASA Access Help Desk at 301–621–0134

- Telephone the NASA Access Help Desk at 301–621–0390

- Write to:
  NASA Access Help Desk
  NASA Center for AeroSpace Information
  7121 Standard Drive
  Hanover, MD 21076

NASA/TM—2001-210461

Structural Analysis of Composite Flywheels: An Integrated NDE and FEM Approach

Ali Abdul-Aziz, George Baaklini, and Jeffrey Trudell
Glenn Research Center, Cleveland, Ohio

Prepared for the
6th Annual International Symposium on NDE for Health Monitoring and Diagnostics
sponsored by The International Society for Optical Engineering
Newport Beach, California, March 4–8, 2001

National Aeronautics and
Space Administration

Glenn Research Center

January 2001

This report contains preliminary findings, subject to revision as analysis proceeds.

Trade names or manufacturers' names are used in this report for identification only. This usage does not constitute an official endorsement, either expressed or implied, by the National Aeronautics and Space Administration.

Available from

NASA Center for Aerospace Information
7121 Standard Drive
Hanover, MD 21076
Price Code: A03

National Technical Information Service
5285 Port Royal Road
Springfield, VA 22100
Price Code: A03

Available electronically at http://gltrs.grc.nasa.gov/GLTRS

STRUCTURAL ANALYSIS OF COMPOSITE FLYWHEELS: AN INTEGRATED NDE AND FEM APPROACH

Ali Abdul-Aziz, George Baaklini, and Jeffrey Trudell
National Aeronautics and Space Administration
Glenn Research Center
Cleveland, Ohio 44135

SUMMARY

A structural assessment by integrating finite-element methods (FEM) and a nondestructive evaluation (NDE) of two flywheel rotor assemblies is presented. Composite rotor A is pancakelike with a solid hub design, and composite rotor B is cylindrical with a hollow hub design. Detailed analyses under combined centrifugal and interference-fit loading are performed. Two- and three-dimensional stress analyses and two-dimensional fracture mechanics analyses are conducted. A comparison of the structural analysis results obtained with those extracted via NDE findings is reported. Contact effects due to press-fit conditions are evaluated. Stress results generated from the finite-element analyses were corroborated with the analytical solution. Cracks due to rotational loading up to 48 000 rpm for rotor A and 34 000 rpm for rotor B were successfully imaged with NDE and predicted with FEM and fracture mechanics analyses. A procedure that extends current structural analysis to a life prediction tool is also defined.

INTRODUCTION

Composite flywheels are being developed as an alternative to expensive and short-life chemical batteries. Flywheels promise orders of magnitude increases in performance and service life in many NASA and military applications, including spacecraft, launch vehicles, aircraft power systems, uninterruptible power supplies, and planetary outposts and rovers (ref. 1). Although the technology holds great promise, there remain a number of challenges to overcome, such as rotor certification for safe life, before these advanced flywheels reach operational status. Carbon-fiber-reinforced polymer composites are the materials of choice for energy applications because of the high energy and power densities that they can achieve (ref. 2). Flywheel design topology can also allow a burst failure mode that is relatively benign in comparison with flywheels made of metallic materials (ref. 3).

A successful deployment of flywheels must address the long-term durability issue of polymer composites due to the limited availability of information about their fatigue characteristics and nonlinear behavior, especially at elevated temperatures. Nondestructive evaluation (NDE) in combination with stress, fracture mechanics, and life prediction models are expected to set a standardized procedure to accurately assess the applicability of using various composite materials to design a suitable rotor-flywheel assembly.

However, for NDE information to be useful in structural characterization and modeling, the NDE data format must be compatible with microstructural and structural models currently being developed (ref. 4). Moreover, to enhance the usefulness of the NDE application, qualitative and quantitative computer analysis tools based on NDE imaging modalities must be developed. Qualitative tools include two- and three-dimensional visualization methods. Quantitative tools include segmentation methods that can send output to commercial finite-element, micromechanical, and/or continuum damage model software (refs. 5 and 6) for the evaluation of composite materials and components.

This report describes the finite-element analyses and the NDE modality undertaken on two flywheel rotors that were spun to burst speed. Computed tomography (CT) and dimensional measurements were used to nondestructively evaluate the rotors before and/or after they were spun to the first crack detection. CT data findings of two- and three-dimensional crack formation were used to conduct finite-element and fracture mechanics analyses. A procedure to extend these analyses to estimate the life of these components is also outlined.

ROTOR TEST CONFIGURATIONS

Two spin-tested rotor configurations were analyzed and scanned. The first was rotor A, a single thick ring that was assembled on a solid aluminum hub. Rotor B, the second configuration, is considered a mass-loaded device. The compressive radial stresses induced by the mass-loading hub help to overcome the poor transverse tensile strength of filament-wound composites; however, the disadvantage is that the circumferential and edge stresses at the inner diameter are increased. The following describes each layout.

1. Pancake rotor assembly A was assembled by U.S. Flywheel Systems, Inc.[1] and the composite rim was manufactured by Toray Fiber, Inc.[2] The rim inside diameter (id) is 6.9 in., the outside diameter is 11.5 in., and the height is 1 in. (fig. 1). The rim is made of M30G carbon fiber and an epoxy resin system. The radial interference fit between the rotor rim and the solid aluminum hub is 0.014 in.
2. Composite rotor assembly B was manufactured by U.S. Flywheel Systems and is shown in figure 2. Rotor B has an approximate inside diameter of 6.9 in., an outside diameter of 10.5 in., and a height of 8.5 in. The aluminum hub is designed to mass load the rim and with the addition of an interference fit, to reduce the peak radial tensile stresses. The rim is made of Hexel's IM7 carbon and AS4D carbon fiber and a shell epoxy resin mixture. The composite rotor rim is 78.3 percent fiber by weight and 71 percent by volume. IM7 fiber was wound at the inner diameter and outer diameter with AS4D fiber in the central portion. The radial interference fit between the composite rotor rim and the aluminum hub is 0.013 in.

FINITE-ELEMENT ANALYSIS

The loading state of a flywheel includes centrifugal, interference, thermal, and residual stresses. For axisymmetric rotors, analytical solutions are available to solve for the rotor stress state. Timoshenko (ref. 7) provided the derivation of the stress state in a cylinder subjected to internal and external pressures, temperature, and centrifugal loading. In Manson (ref. 8), the axisymmetric stress distribution is solved via finite-difference techniques and accounts for height, density, modulus, and temperature variations as a function of radius. Genta (ref. 9) modified Manson's procedure to include orthotropic materials. Gabrys (ref. 10) provides a simple way to solve for the rotor stress state by superimposing anisotropic elasticity analytical solutions. Gabrys also provides a simple method to predict residual stresses that result from the fabrication process and the experimental correlation of the flywheel ring coefficient of thermal expansion.

The superimposed solutions assume plane stress and are only applicable for constant-axial-height, cylindrically orthotropic flywheels. Finite-element analyses are performed when the rotors or applied loads are not axisymmetric or if fracture mechanics analysis is to be performed. The ANSYS (ref. 11) finite-element code was used to solve the nonlinear, two- and three-dimensional contact analysis, whereas the two-dimensional stress and fracture mechanics analyses were performed with MARC (ref. 12). The two- and three-dimensional, finite-element models were generated using MSC/Patran Graphics (ref. 13) and ANSYS GUI, and inputs were generated for each FE code accordingly. The ANSYS Parametric Design Language (ADPL) was implemented to automatic nonlinear solution and data recovery with parametric changes in geometry, material, mesh, boundary conditions, and loads.

Pancake Rotor A

The MARC pancake rotor A model consisted of 995 nodes and 912 quad4 elements and is shown in figure 3. The choice of the planar representation (plane stress) of a disk allows analysis of nonaxisymmetric rotors (i.e., bolt holes for hub-shaft attachment). An alternative approach would use axisymmetric elements to account for variations in the radial and hoop stresses as a function of axial height and would decrease the required number of elements and run time. The nodes modeling the contact were intentionally offset in the hoop direction and were not radially aligned to accommodate the contact condition set by the MARC code. The ANSYS pancake rotor A model consisted of 7065 nodes and 7290 PLANE42 and CONTACT48 elements and is shown in figure 4. A large number of elements was generated as run times were only a minute or two and peak stress locations are resolved more

[1]U.S. Flywheel Systems, Newberry Park, CA 91320.
[2]Toray Fiber, Inc., Tacoma, WA 98446.

accurately; however, fewer elements by an order of magnitude would give similar results. Using Genta's method coded in FORTRAN, the axisymmetric stress distribution of the rotor A was solved and compared with the two-dimensional solutions of MARC and ANSYS to benchmark the modeling approaches.

Rotor B

The second mass-loaded hub was modeled in both two and three dimensions, which provided guidance to perform the fracture mechanics analysis in two dimensions. Both finite-element method (FEM) codes, ANSYS, and MARC were utilized to conduct these analyses. The rim stress distribution is clearly three dimensional due to the axial counterbore and its 1/8th cyclic symmetry, creating a nonuniform axial and circumferential mass loading of the hub. The three-dimensional model consists of 1642 eight-node brick elements and 2283 nodes and is shown in figure 5. Only half the axial height was included in the model and the X,Y-plane nodes were constrained in the Z-direction to represent axial symmetry. The two-dimensional-model assembly consists of 1408 quad4 and quad8 elements and 2592 nodes and is shown in figure 6. The two reasons for using both quad4 and quad8 elements to model the rim were that (1) quad4 elements are needed to model the contact region between the hub and rim since higher order elements are not suitable for contact analysis because of a mismatch in stiffness between midside and corner nodes and (2) quad8 elements are required for subsequent fracture mechanics analysis. This however creates a region in which there is a stiffness mismatch between midside and corner nodes, although it is a region of low radial stress and not at the contact surface. Quarter symmetry was chosen to facilitate the application of boundary conditions to the X,Y-axes.

The material properties listed in table I were used for the analyses. The composite properties were generated using the software ICAN (Integrated Composite Analyzer, ref. 14) because coupon test data were not available. Orthotropic and directionality effects of the material properties were all accounted for in the analyses.

In performing the analysis, the applied load is divided into a series of small incremental steps to aid in reaching a converging solution and to avoid encountering mathematical instabilities typically during contact. However, the first load step includes the full amount of interference, with successive load steps applying small increments of all other applied loads.

FRACTURE MECHANICS

To conduct the fracture mechanics analysis, the J-integral parametric option available in the MARC code was applied, resulting in the calculation of the change in strain energy due to nodal movement near the crack tip. This quantity is evaluated by numerical integration at each increment for each prescribed nodal movement to determine the derivative of the strain energy with respect to the crack length at the end of each increment.

In addition to overcoming the difficulty that is usually encountered in the finite-element fracture mechanics representation of the solution near the crack tip, the mesh must be modeled so that the singularity is approximated with sufficient accuracy. Many methods have been established to arrive at such an approximation; however, the most commonly employed uses a degenerate form of the standard eight-node quadrilateral element. This method, usually referred to as the "1/4-point node technique" (ref. 15), is also preferred for analyses conducted with the MARC code (ref. 12). It is applied by using an eight-node quarter of the edge length, the edge opposite the crack being kept straight. When these steps are followed, a singularity in the stress field exists in all directions going outward radially from the crack tip.

STRESS INTENSITY FACTOR

The calculation of the stress intensity factor K will allow one to determine at which load increment crack propagation occurs. This is done by calculating the elastic-plastic energy release rate, which is confined to a single parameter: the strength of the singularity in the elastic-plastic stress field at the crack tip. The magnitude of K depends on the crack length, the distribution and intensity of applied loads, and the geometry of the structure. Crack propagation will occur when any combination of these factors causes K to be equal to or greater than the experimentally determined material threshold value (ref. 16). The equation that relates K to the energy release rate is (ref. 12)

$$G = \frac{\mathrm{d}W}{\mathrm{d}A} = \frac{K^2}{E} \tag{1}$$

where G is the energy release rate during a small crack extension; W is the strain energy in pounds force per inch per inch; K is the stress intensity factor in thousands of pounds per square inch (kpsi); $A = a \times b$ where a and b are the crack length and width in inches, respectively; and E is the modulus in thousands of pounds per square inch (kpsi).

The stress intensity factor is given by

$$K = \sqrt{E\frac{\mathrm{d}W}{\mathrm{d}A}} \tag{2}$$

After the functional forms of K have been determined, the state of the stress and displacement near the crack tip region of the structure can be determined. It must be noted, however, that these equations represent a specific provision that describes the general approach to identifying these key parameters. Thus, for polymer matrix composites some modification will be required.

The life prediction computation is based on obtaining the data from the analysis and then applying the Paris relation, which ties the number of life cycles to the crack length and the stress intensity factor (ref. 17) and is described by

$$\mathrm{d}N = \frac{\mathrm{d}a}{c(\Delta K)^n} \tag{3}$$

where N is the number of loading cycles, da is the incremental crack length, c and n are material constants determined from experimental data, and ΔK is the stress intensity factor range ($K_{max} - K_{min}$). The loading cycle is defined as a combination of the press fit and the rotational speed loading.

Equations (1) to (3) identify a procedure that would lead to life assessment calculations. However, a fatigue crack growth data base would have to be established for these materials to perform a life estimate.

RESULTS AND DISCUSSION

The results generated are presented in this section, which includes details covering each rotor assembly and the corresponding stress output.

Rotor A

The radial and hoop stress distributions of the pancake rotor assembly as predicted by the MARC code are shown in figures 7 to 10 for the entire rotor and for the rim section only. The peak hoop stress is 141 kpsi at the rim contact region with the hub (fig. 9). The peak radial stress of 3.4 kpsi occurs at a radial location of 4.35 in. as indicated in figure 10. These stresses were generated at a rotational speed of 48 000 rpm.

The radial and hoop stress distributions as calculated by ANSYS are shown in figures 11 and 12. The peak radial stress is 3.52 kpsi and the peak hoop stress 135.30 kpsi. The nodal peak radial stress occurred at a location of approximately 1.38 in. (nodal spacing was 0.115) from the inside diameter of the 2.3-in.-thick rim. The variation in radial stress versus radius for several speeds is shown in figure 13. Note that the location of peak radial stress moves from the outer radius to the center as speed increases because the centrifugal loading continues to offset the compressive preload during assembly. Generally, carbon fiber exhibits an out-of-plane radial strength of 3 to 10 kpsi and 200 to 300 kpsi in the hoop direction (ref. 18). However, the processing technique for the composite materials addressed in this work must be verified in order for these provisions to be held valid.

The results of Genta's modification of Manson's finite-difference method are shown in table II. Note that the rim peak radial stress is predicted to be 3.52 kpsi at a radial location of 4.83 in. (1.38 in. from the rim id), which is in excellent agreement with the ANSYS and MARC results. The fiber volume ratio (FVR) was then reduced to 0.63 (but the same density of 0.69 FVR was assumed) to show the sensitivity of reduced stiffness (due to translational inefficiencies, fatigue effects, variations in fiber and matrix properties) on the peak radial stress location. The peak radial stress increased to 3.76 kpsi at the radial location of 4.78 in. (1.33 in. from the rim id), a shift of 0.05 in. from the 0.69-FVR results. The peak hoop stress decreased to 126.9 from 135.5 kpsi. An estimate of residual stress was then made (no measurements) based upon the cure cycle of the manufactured ring, and peak radial stress increased to 6.4 kpsi at the radial location of 4.67 in. (1.23 in. from the rim id). The residual stress shifted the location of peak radial stress 0.15 in. versus 0.05 in. for a 7-percent change in stiffness.

NDE Findings Versus FEM of Rotor A

As reported in the previous paragraph, the finite-element analyses (FEA) of the rotor assembly uncovered the stress levels experienced by the unit as a result of the high rotational loading. After spin testing to 48 000 rpm, CT images were taken to identify structural damage. Figure 14 shows a CT scan of the rotor after it was spun. An evaluation of the CT image indicated a cracking of the rotor along the entire circumferential direction. The crack is nearly symmetrical and is located at a 4.465-in. radial distance. The finite-element analysis reported in figures 10 and 11 showed that the maximum radial stress region is at a radial distance range of 4.35 to 5.34 in. Furthermore, the peak radial stress occurred at 4.78 in. or with the addition of estimated residual stress, at 4.67 in. With a 7-percent stiffness reduction, the crack would move farther toward the center of the rim to 4.62 in. Because of the symmetrical nature of the crack, with accurate estimates or measurements of stiffness and residual stress and assuming no localized stress concentrations, the stress analysis can be correlated to crack location observed by the CT scan, which corroborates that the FEA is in good agreement with the NDE findings. In addition, both procedures demonstrated that obtaining parallel results from both methods is achievable. Additionally, these findings constitute an additional means of verifying and confirming service-related damage and design anomalies typically experienced by various structural components.

Mass-Loaded Hub Rotor B

Figures 15 and 16 illustrate the two-dimensional radial stresses and the hoop stresses for the rotor. The stress distribution as shown in figure 15 is the result of a complicated combined press-fit centrifugal loading on a nonaxisymmetric structure. Higher hoop stresses are generated at the rim-hub interface as a result of the contact effects or mass loading of the hub onto the rim. The corresponding stress magnitude reached 94 kpsi. The radial stress profile in figure 16 shows that the maximum stress level in the hub is in the hub holes, which is an indication that the hub is very likely to fail at that particular section if a higher rotational load is applied. A nonuniform radial stress distribution shown in the rim near the hub-rim interface has developed because quad8 and quad4 elements were used, creating a mismatch in stiffness between the midside and corner nodes. The nonuniform stress distribution also created convergence problems and tremendous increases in CPU times.

Figure 17 shows the three-dimensional hoop stress distribution generated in the flywheel at 34 000 rpm, the speed at which the first crack developed in the rim. Note that the hoop stress reaches a maximum value of 113 kpsi at the area of contact between the rim and the hub. The radial stress distribution at 34 000 rpm is shown in figure 18. As expected, the peak radial stress is again in the hub holes. Figure 19 shows the Von Mises stresses in the hub with a stress level of 32.4 kpsi at the region adjacent to the holes.

Figure 20 illustrates the three-dimensional hoop stresses for the rim only at 34 000 rpm. Note that a nonuniform hoop stress distribution is clearly shown. The maximum hoop stress occurs at the axial region below the counterbore of the hub, which can be explained by examining the radial stress distribution. Figure 21 illustrates the three-dimensional radial stresses. Note the axial shift in radial stress due to the counterbore in the hub, which is also illustrated at 0° and 30° in figures 22 and 23. The compressive radial stresses at the rim inner radius decrease axially from the center to the top edge, but this higher radial preload induces higher hoop stresses in the center than in the top edge.

The peak hoop stress distribution will be reversed as the speed is increased because the centrifugal forces decrease the initial interference preload near the center, and the counterbore mass-loading region of the hub induces higher compressive radial stresses. The mass loading of the counterbore section of the hub will also create higher bending stresses in the rim than that of a solid hub design, and shear stress levels will have to be addressed at the higher speeds. With regard to radial stress magnitude, the peak is about 0.3 kpsi at a radial distance of 5.51 in. (fig. 21). The radial stress, when combined with estimated residual stresses, appears to be at the lower bound of the expected transverse strength levels and indicates a critical value that causes failure. Residual stresses will increase and shift the peak radial stresses inward toward the center of the rim as would the decreased hoop stiffness that was described in the previous section.

Figure 24 represents the two-dimensional radial stress distribution of the rotor obtained from the fracture mechanics analysis at a rotational speed of 34 000 rpm. Figure 25 duplicates figure 24 with the exception that it illustrates a closer view of the crack propagation generated. The crack was propagated at the nodal point of the element that exhibited the highest stress as indicated by an earlier three-dimensional stress analysis. An initial crack size of 0.005 in. was assumed based upon both data suggested by the CT scan and visual inspection. Furthermore, the crack collected through the CT scan was asymmetric and it replicated the phenomena experienced by the flywheel while undergoing excessive centrifugal loading. In this work, however, to simplify the analytical calculations, the two-dimensional analyses assumed that the crack was being propagated symmetrically with respect to the radial direction and along the circumference of the flywheel.

Additional observations noted in viewing figure 25 are confined to the fact that the stress magnitude at the crack tip grew higher as the crack advanced. The counterbore in the hub is primarily responsible for the high rim bending stresses that contributed to the rotor cracking. Figure 26 presents the energy release rate versus the crack length. A highlighted linear variation (as anticipated) shows that the higher the energy rate, the higher the crack length. Furthermore, this denotes that a higher energy release rate would ultimately lead to unstable crack growth provided that the fracture toughness data of the material demonstrate such a possibility. This scenario will drive the crack to grow until it hits the edge or boundaries. Moreover, this information provides a preliminary guide for performing life analyses when fatigue crack growth data for these materials become available.

NDE Findings Versus FEM of Rotor B

The NDE-FEA results for rotor B are presented in this section. Figure 25 shows a computed CT scan for the rotor. The scan is a cross-sectional view taken in a direction parallel to the axis of rotation. The defects detected by the CT scan clearly show the two cracks, which vary in axial location because of the variation in the radial stress profile created by the mass-loaded hub and the rotational speed of 34 000 rpm. The view indicates that the cracks are parallel to the rotor axis of rotation, they are asymmetrical along the entire radial direction, and they fall within 5.33 to 5.81 in. at the middle section of the rotor. These data are in close agreement with the FEA data without residual stresses, which initiated peak radial stresses at a radial distance of 5.51 to 6.12 in. These findings supported the fact that starting crack propagation at that particular location via the fracture mechanics analysis was consistent with the CT data.

Other supporting data relating NDE to FEA are seen in figures 23 and 27. For instance, the stress results shown in figure 23, which represents the radial stresses in the rim, clearly indicate that the maximum stress region is within the section defined by the CT scan. Figure 23 describes the stress region at the contact side with the hollow hub whereas figure 27 shows the crack locations and variations within the rim. The measurements reported, as obtained from figure 27, once more show that the NDE data correlate well with those predicted by the FEA.

Looking at the data collected from the CT scan and the FEA results allows us to conclude that with a good degree of accuracy, it was possible to detect the crack origination area and its direction. Furthermore, the NDE data assisted us in performing a three-dimensional, finite-element analysis to identify the crack and the maximum stress locations. Such information was greatly needed to grow a crack in the rim for life prediction purposes.

CONCLUSIONS

Two- and three-dimensional, finite-element stress analyses were conducted for two flywheel rotor systems with solid and hollow hubs, respectively. Subsequent two-dimensional fracture mechanics analysis were conducted to trace a crack propagation identified by computed tomography (CT) scans after spin loading to 34 000 rpm. The results were discussed and compared with those predicted by CT. The following conclusions are drawn:

1. The finite-element analyses (FEA) showed that the rotor first crack as detected by the CT scan can be modeled with finite elements provided that the material properties and residual loads are adequately quantified.
2. Indepth FEA modeling and evaluation of two flywheel rotor systems under spin loading conditions was successfully conducted.
3. Crack location cited via CT corresponded well with that simulated by the fracture mechanics analysis.
4. Lack of fatigue crack propagation data for the composite materials hindered conducting a life estimate as desired. Until a fatigue crack growth data base is established, conducting a life assessment will remain an unattainable task.
5. An aluminum hub design is a crucial factor affecting the durability of the rotor because an improper hub design can result in high bending stresses that in turn result in complex crack propagation behavior. Therefore, the hub designer must consider bringing the bending stresses to a minimum level.

REFERENCES

1. Ashley, Steven: Flywheels Put a New Spin on Electric Vehicles. Mech. Eng., vol. 115, no. 10, 1993, pp. 44–51.
2. Olszewski, Mitchell, et al.: On the Fly or Under Pressure. Mech. Eng., vol. 110, no. 6, 1988, pp. 50–58.
3. Coppa, A.P.: Flywheel Containment and Safety Considerations: An Assessment of Integrated Flywheel System Technology. NASA CP–2346, 1985, pp. 243–264.
4. Baaklini, George Y., et al.: Structural Characterization of Metal Matrix Composites Using NDE Data. NASA CP–10192. Available from the Subsonic Systems Office, NASA Glenn Research Center, Carol A. Ginty.
5. Wilt, Thomas E.; Arnold, Steven; and Goldberg, Robert: Micromechanics Analysis Code: MAC Features and Applications. NASA CP–10192. Available from the Subsonic Systems Office, NASA Glenn Research Center, Carol A. Ginty.
6. Arnold, Steven M.; and Wilt, Thomas E.: Deformation and Life Prediction of Circumferentially Reinforced SCS-6/Ti-15-3 Ring. NASA RP–1361, Erwin V. Zaretsky, ed., 1996, pp. 51–60.
7. Timoshenko, Stephen; and Goodier, J.N.: Theory of Elasticity. McGraw-Hill, New York, NY, 1970.
8. Manson, S.S.: Determination of Elastic Stresses in Gas-Turbine Disks. NACA TN–1279, 1947.
9. Genta, G.: Kinetic Energy Storage: Theory and Practice of Advanced Flywheel Systems. Butterworths, London, England, 1985.
10. Gabrys, Christopher Walter: Design, Fabrication and Testing of Advanced Composite Energy Storage Flywheels (Filaments, Urethane Matrix). Ph.D. Dissertation, Pennsylvania State University, 1996.
11. ANSYS Finite Element Program. ANSYS Release 5.4, ANSYS, Inc., Canonsburg, PA, 1997.
12. MARC General Purposes Finite Element Analysis Program. Vol. A: User Information Manual; Vol. F: Theoretical Manual. MARC Analysis Research Corporation, Palo Alto, CA, 1996.
13. MSC/PATRAN Graphics and Finite Element Package. Vols. I and II. The MacNeal-Schwendler Corporation, Costa Mesa, CA, 1997.
14. Murthy, P.L.N.; and Chamis, C.C.: Integrated Composite Analyzer (ICAN): Users and Programmers Manual. NASA TP–2515, 1986.
15. Nagtegaal, J.C.; and deJong, J.E.: Some Computational Aspects of Elastic-Plastic Large Strain Analysis. Int. J. Numer. Methods Eng., vol. 17, no. 1, 1981, pp. 15-41.

16. Rice, J.R.; and Tracy, D.M.: Computational Fracture Mechanics. Proceedings of the Symposium on Numerical and Computer Methods in Structural Mechanics, S.J. Fenves, et al., eds., Academic Press, New York, 1973, pp. 585–623.
17. Paris, P.; and F. Erdogan: A Critical Analysis of Crack Propagation Laws. J. Basic Eng. Trans. ASME, vol. 85, 1963, pp. 528–534.
18. Agarwal, Bhagwan D.; and Broutman, Lawrence J.: Analysis and Performance of Fiber Composites. Second ed., John Wiley & Sons, Inc., New York, NY, 1990.

TABLE I.—FIBER AND COMPOSITES MATERIAL PROPERTIES

Properties	Aluminum	AS4D	IM7	M30G
Density, lb/in.^{3}	0.1010	0.0584	0.0584	0.0567
Modulus of elasticity, *E*, kpsi				
E_{11}	10.4×10^3	13.6×10^2	13.6×10^2	13.3×10^2
E_{22}	----------	29.6×10^3	27.8×10^3	29.6×10^3
E_{33}	----------	13.6×10^2	13.6×10^2	13.3×10^2
Poisson's ratio, ν				
ν_{12}	0.30	0.013	0.012	0.011
ν_{21}	-----	.24	.24	.25
ν_{13}	-----	.38	.39	.39
Energy release rate, *G*, kpsi				
G_{11}	-----	6.68×10^2	6.68×10^2	6.44×10^2
G_{22}	-----	6.68×10^2	6.68×10^2	6.44×10^2
G_{33}	-----	3.89×10^2	3.89×10^2	3.76×10^2

TABLE II.—PANCAKE ROTOR STRESS:STRAIN DISTRIBUTION USING GENTA'S METHOD (REF. 9)

Pancake M30G 6.9"ID 11.5"OD

Element and Material Characteristics

Station	Radius	Height	Tap	Ec	Er	v	rho	
0	.000	1.000	1	.1070E+08	.1070E+08	.32	.2617E-03	AL7075-T6
1	3.450	1.000	1	.1070E+08	.1070E+08	.32	.2617E-03	AL7075-T6
2	3.450	1.000	1	.2962E+08	.1326E+07	.25	.1471E-03	fwm30gfv69
3	5.750	1.000	1	.2962E+08	.1326E+07	.25	.1471E-03	fwm30gfv69

BC: Pressure and Interference

Station	Radius	Height	Pressure	Interference
0	.000	1.000	.0	.00000
1	3.450	1.000	.0	.00000
2	3.450	1.000	.0	.00000
3	5.750	1.000	.0	.00000

Disk Stress Analysis Using Manson's Procedure - LU Solid Disk

Inner radius [in.]	=	.000
Outer radius [in.]	=	5.750
Mass	=	.0196
Moment of inertia	=	.2780
Angular velocity [rpm]	=	48000.0
Angular velocity [rad/s]	=	5026.5
Initial stress [inner hub]	=	.0
Number of stations	=	4
Number of elements/station	=	50
Number of elements	=	150

Temperature and Thermal Data

Station	Radius	Thick	Temp	Alpha R	Alpha C
0	.000	1.000	312.2	.1300E-04	.1300E-04
1	3.450	1.000	312.2	.1300E-04	.1300E-04
2	3.450	1.000	.0	-.3600E-06	.1460E-04
3	5.750	1.000	.0	-.3600E-06	.1460E-04

Stress Distribution

Station	Radius	Height	Sr (ksi)	Sc	Von Mises
0	.000	1.000	22368.9	22368.9	22368.9
50	3.450	1.000	-10312.6	3066.8	12140.1
100	3.450	1.000	-10312.6	135297.9	140737.9
150	5.750	1.000	.0	79725.2	79725.2

Strain/Displacement Distribution

Station	Radius	Height	er	ec	ur
0	.000	1.000	.005480	.005480	.000000
50	3.450	1.000	.003003	.004654	.016055
100	3.450	1.000	-.008903	.004654	.016055
150	5.750	1.000	-.000663	.002692	.015477

Max/Min Stress Distribution - Each Station

Station	Radius	SrMax	SrMin	ScMax	ScMin
0	.000	22.4	22.4	22.4	22.4
1	3.450	22.4	-10.3	22.4	3.1
2	3.450	-10.3	-10.3	135.3	5.1
3	5.750	3.5	-9.0	130.5	79.7

Max/Min Strain Distribution - Each Assembly

		AL7075-T6 Strain			fwm30gfv69 Strain		Strain	
KRPM	PRELOAD	Radial	Hoop	VM	Radial	Hoop	Radial	Hoop
48.00	312.2F Max	.0055	.0055	.0055	.0029	.0047		
48.00	312.2F Min	.0030	.0047	.0041	-.0089	.0027		

Max/Min Displacement Distribution - Each Assembly

		AL7075-T6 Displacement		fwm30gfv69 Displacement		Displacement	
KRPM	PRELOAD	Radial	Hoop	Radial	Hoop	Radial	Hoop
48.00	312.2F Max	.0161	.0000	.0161	.0000		
48.00	312.2F Min	.0000	.0000	.0136	.0000		

Max/MIN Stress Distribution - Each Assembly

		AL7075-T6 Stress			fwm30gfv6 Stress		Stress	
KRPM	PRELOAD	Radial	Hoop	VM	Radial	Hoop	Radial	Hoop
48.00	312.2F Max	22.37	22.37	22.37	3.52	135.30		
48.00	312.2F Min	-10.31	3.07	9.11	-10.31	5.11		

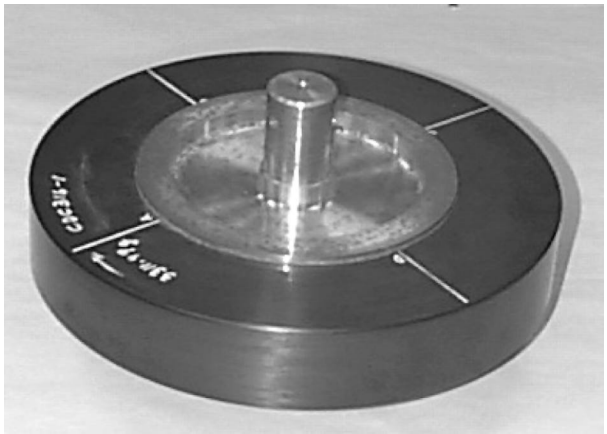

Figure 1.—Pancake rotor assembly A with aluminum hub.

Figure 2.—Composite rotor assembly B.

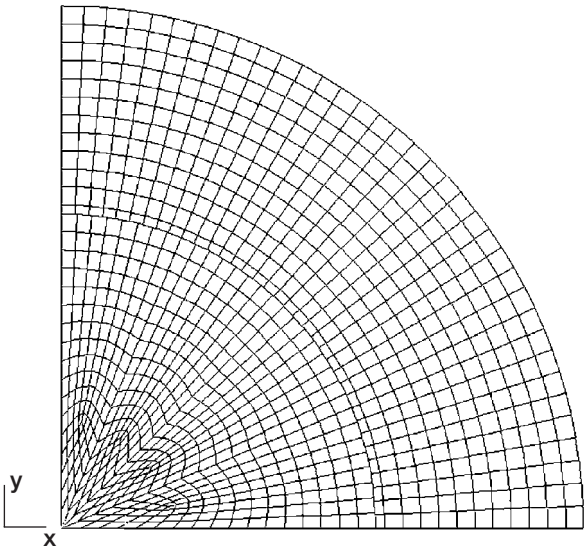

Figure 3.—Pancake rotor A two-dimensional, finite-element model consisting of 912 quad4 elements and 995 nodes. Based on MARC analysis.

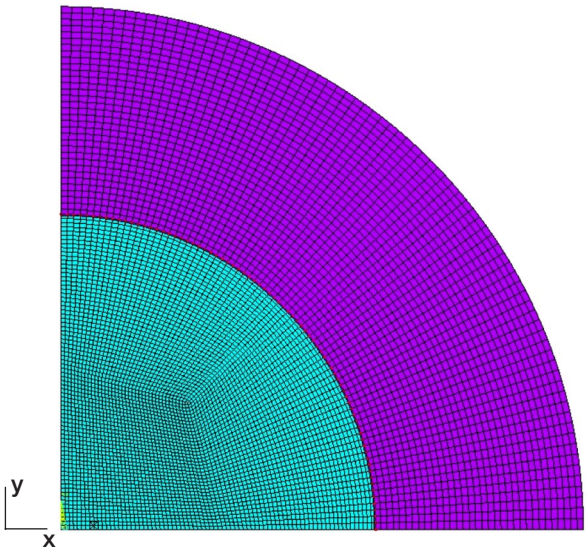

Figure 4.—Pancake rotor A two-dimensional, finite-element model consisting of 7065 nodes and 7290 PLANE42 elements. Based on ANSYS analysis.

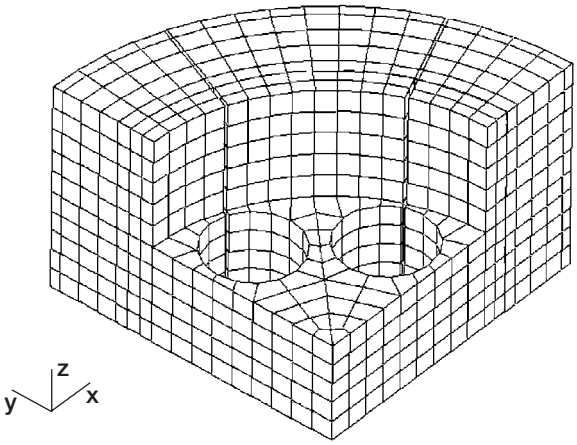

Figure 5.—Rotor B three-dimensional, finite-element model consisting of 1642 eight-node brick elements and 2283 nodes.

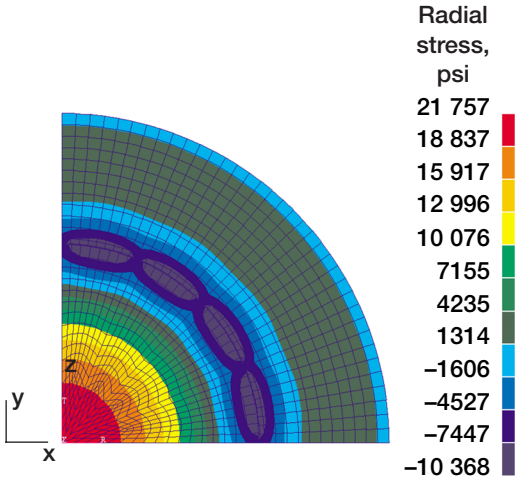

Figure 7.—Radial stress distribution for rotor A based on MARC analysis. Rotational speed, 48 000 rpm.

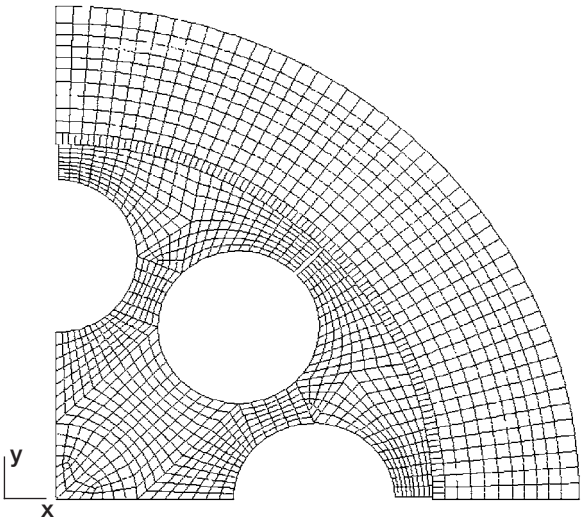

Figure 6.— Rotor B two-dimensional, finite-element model consisting of 1408 quad4 and quad8 elements and 2592 nodes.

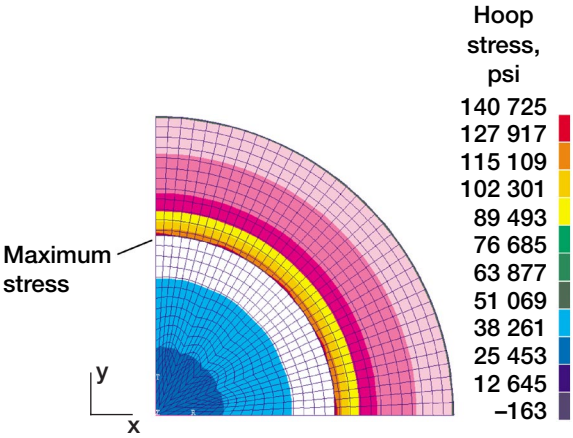

Figure 8.—Hoop stress distribution for rotor A based on MARC analysis. Rotational speed, 48 000 rpm.

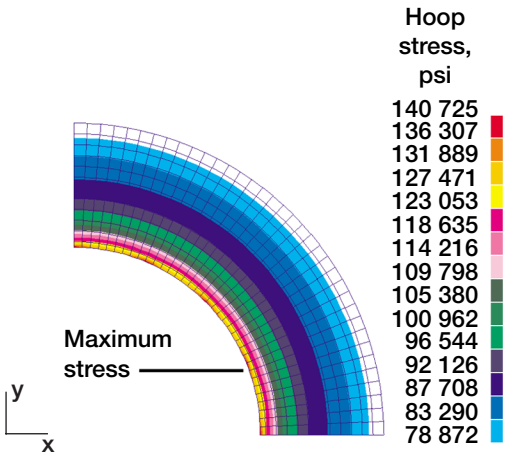

Figure 9.—Rim hoop stress distribution for rotor A based on MARC analysis. Rotational speed, 48 000 rpm.

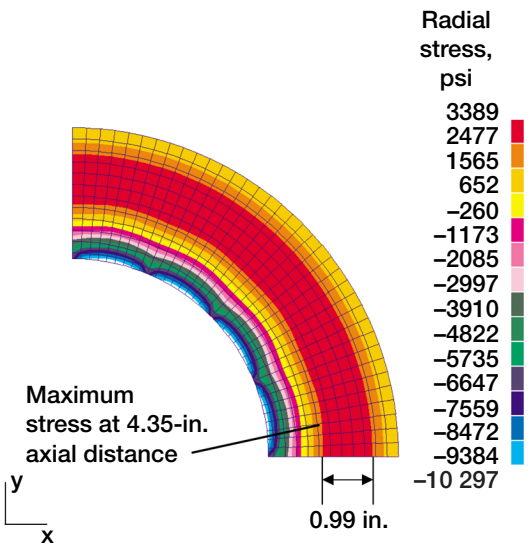

Figure 10.—Rim radial stress distribution for rotor A based on MARC analysis. Rotational speed, 48 000 rpm.

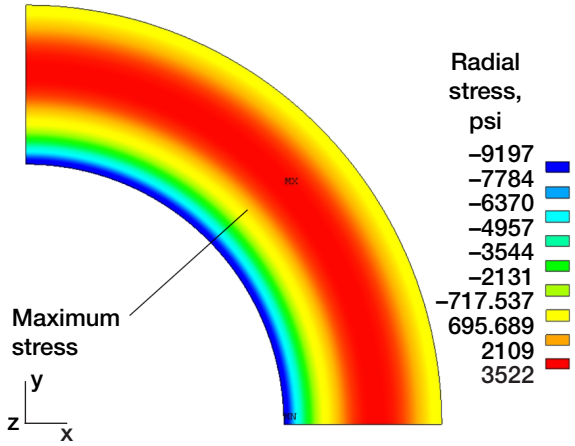

Figure 11.—Rim radial stress distribution for rotor A based on ANSYS analysis. Rotational speed, 48 000 rpm.

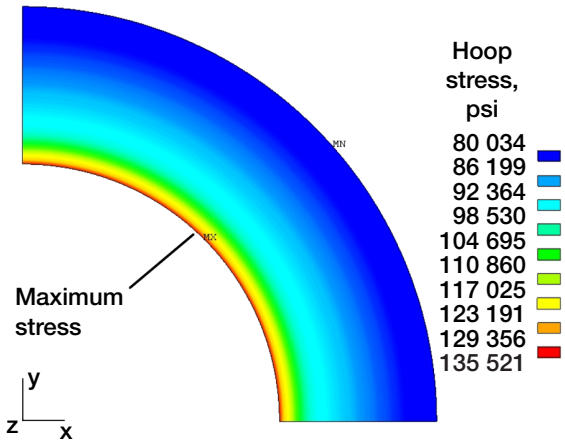

Figure 12.—Rim hoop stress distribution for rotor A based on ANSYS analysis. Rotational speed, 48 000 rpm.

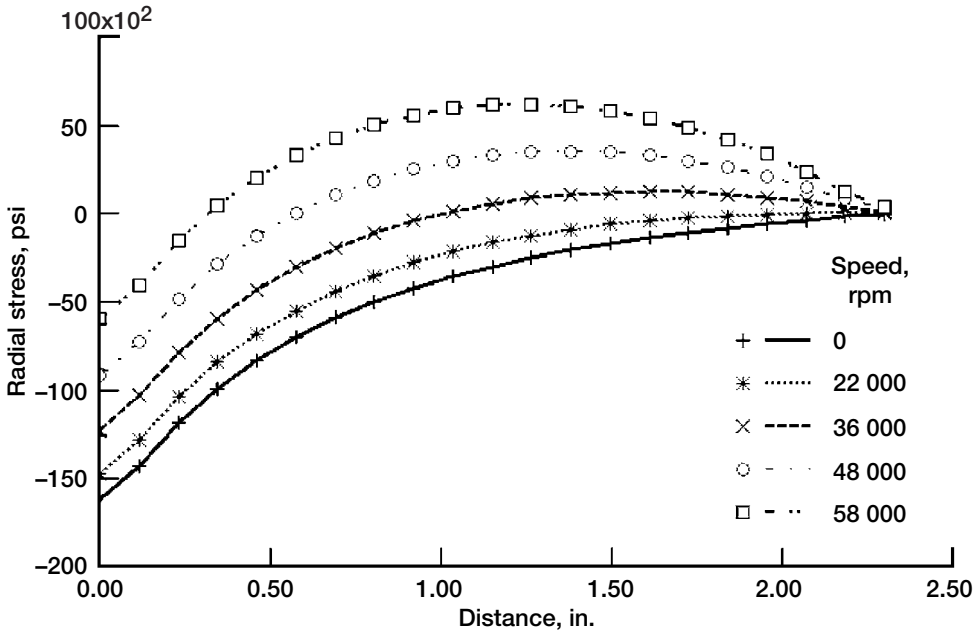

Figure 13.—Rim radial stress distribution as function of radius at several speeds for rotor A based on ANSYS analysis.

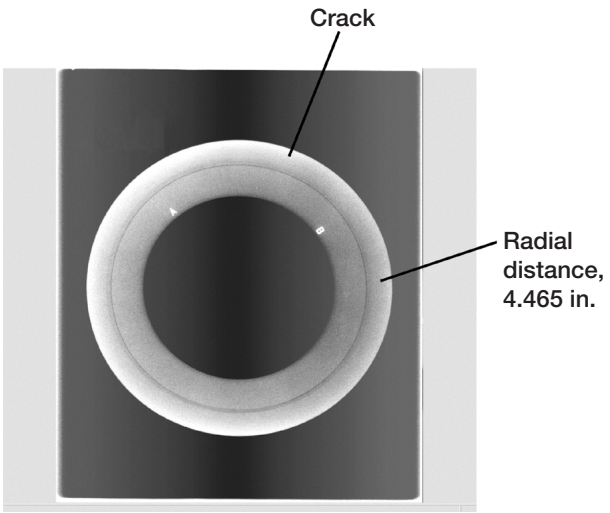

Figure 14.—Computed tomography scan of tested pancake rotor A.

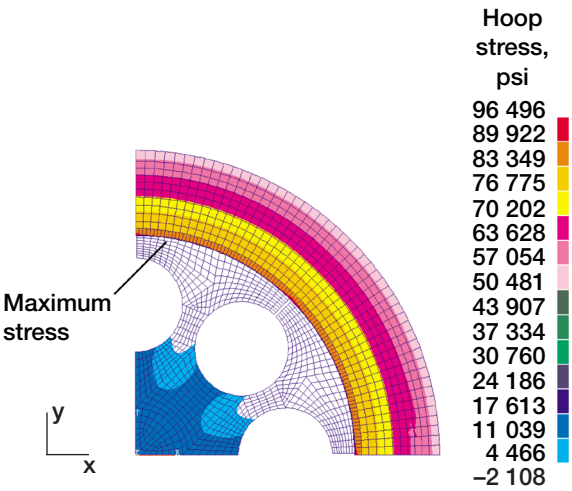

Figure 15.—Hoop stress distribution for rotor B based on MARC two-dimensional analysis. Rotational speed, 34 000 rpm.

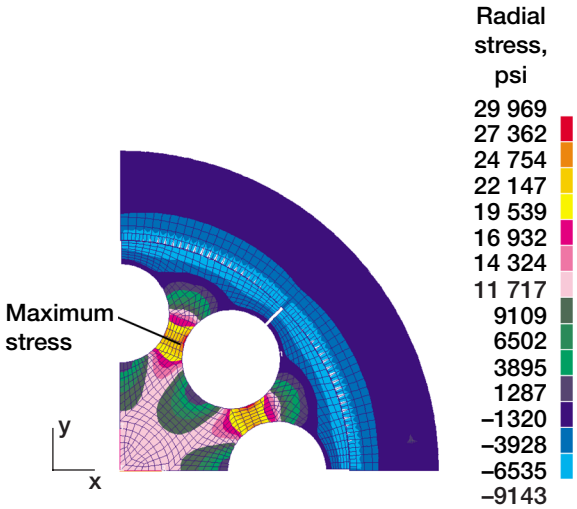

Figure 16.—Radial stress distribution for rotor B based on MARC two-dimensional analysis. Rotational speed, 34 000 rpm.

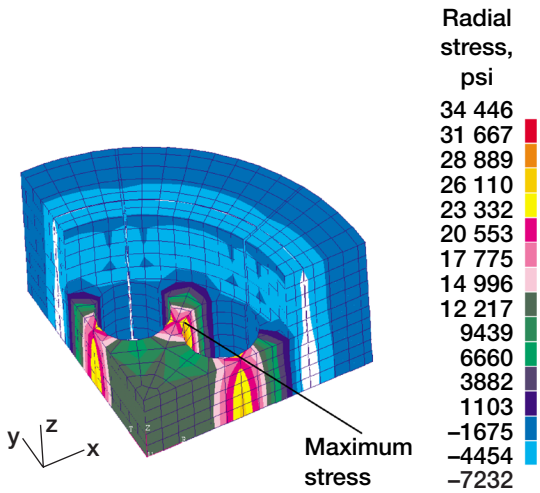

Figure 18.—Radial stress distribution for rotor B based on ANSYS three-dimensional, finite-element analysis. Rotational speed, 34 000 rpm.

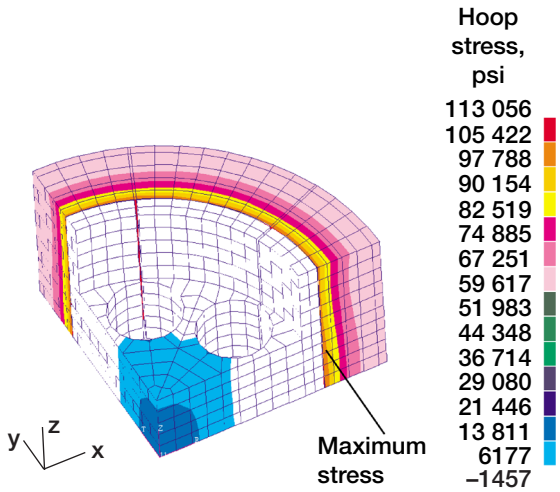

Figure 17.—Hoop stress distribution for rotor B based on ANSYS three-dimensional, finite-element analysis. Rotational speed, 34 000 rpm.

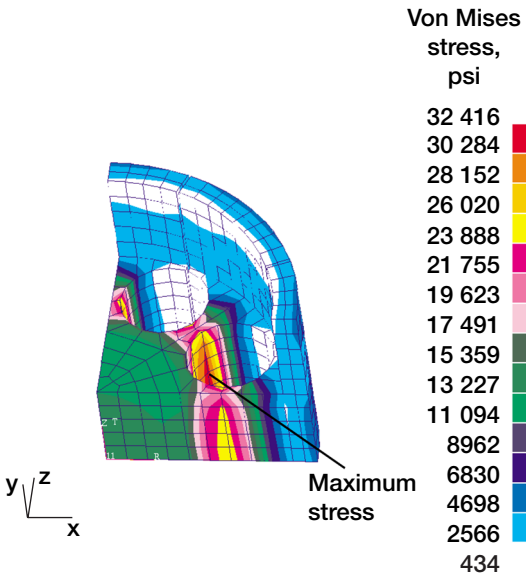

Figure 19.—Von Mises stress distribution for hub of rotor B based on ANSYS three-dimensional, finite-element analysis. Rotational speed, 34 000 rpm.

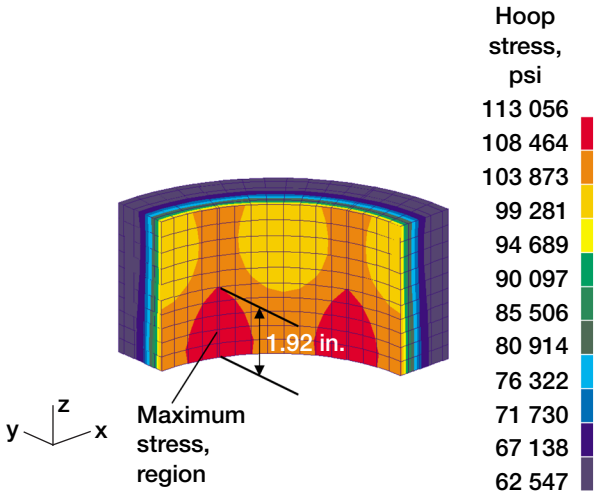

Figure 20.—Rim hoop stress distribution for rotor B based on ANSYS three-dimensional, finite-element analysis. Rotational speed, 34 000 rpm.

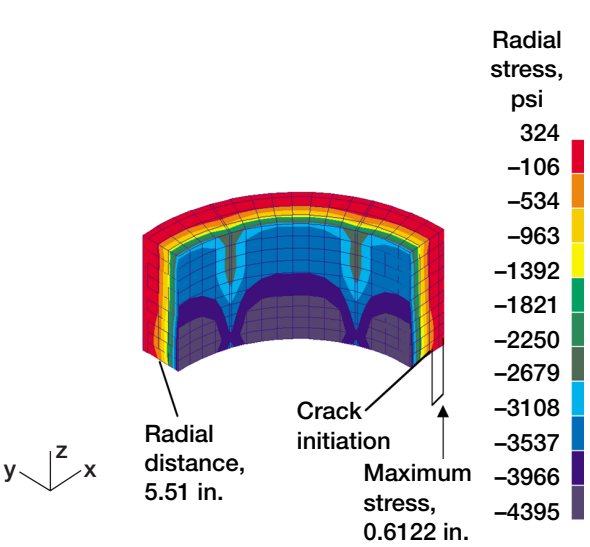

Figure 21.—Rim radial stress distribution for rotor B based on ANSYS three-dimensional, finite-element analysis. Rotational speed, 34 000 rpm.

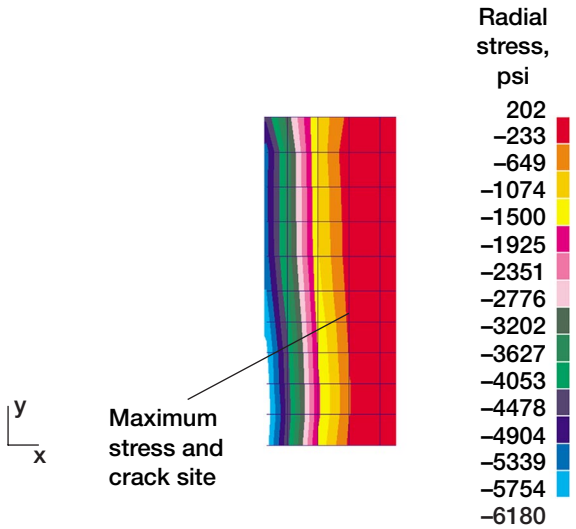

Figure 22.—Rim radial stress distribution for rotor B 0° slice based on ANSYS three-dimensional, finite-element analysis. Rotational speed, 34 000 rpm.

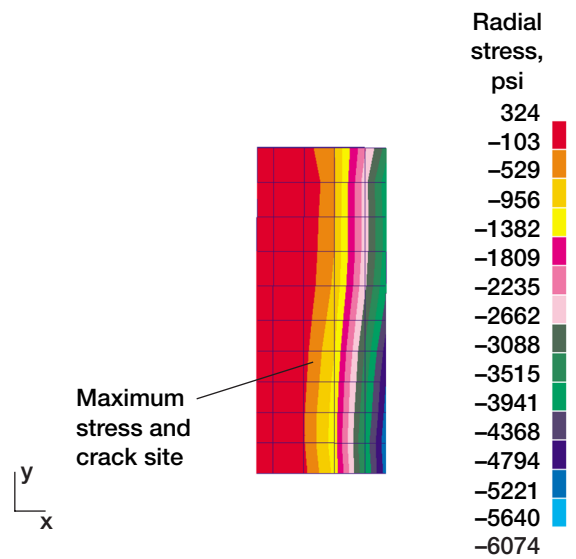

Figure 23.—Rim radial stress distribution for rotor B 30° slice based on ANSYS three-dimensional, finite-element analysis. Rotational speed, 34 000 rpm.

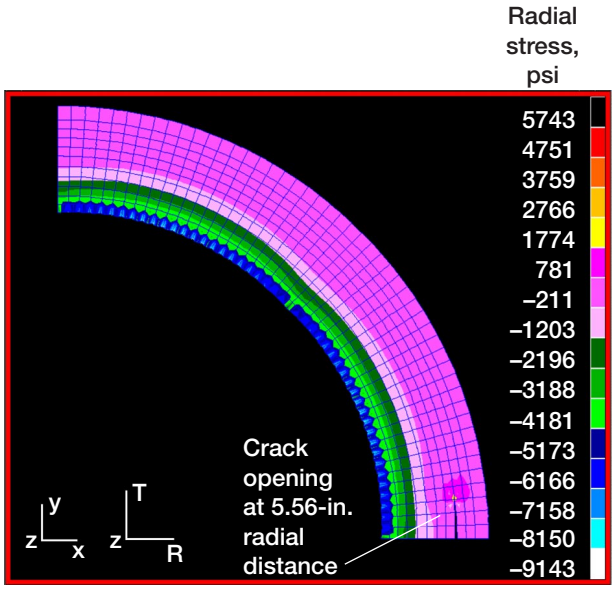

Figure 24.—Rim fracture mechanics radial stress distribution for rotor B based on MARC analysis. Rotational speed, 34 000 rpm.

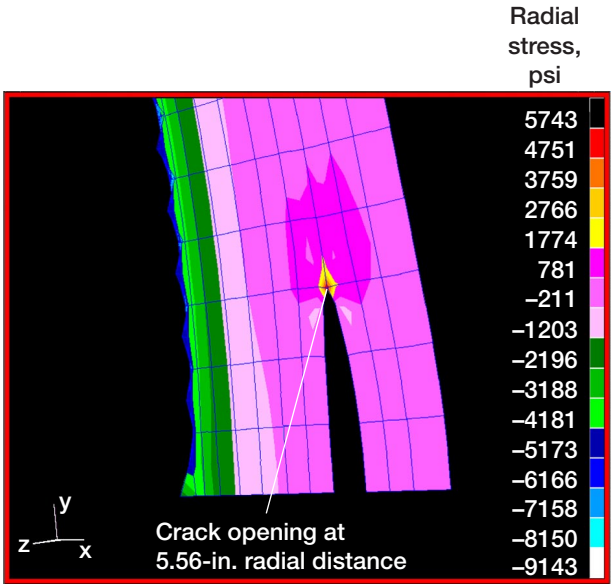

Figure 25.—Rim fracture mechanics radial stress distribution for rotor B based on MARC analysis. Rotational speed 34 000 rpm (closeup view of crack propagation).

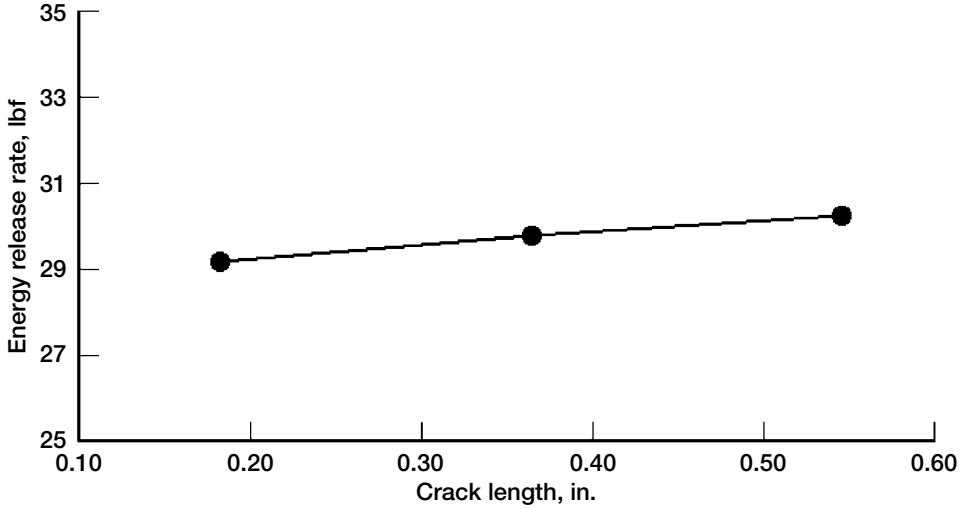

Figure 26.—Energy release rate as function of crack length for rotor B.

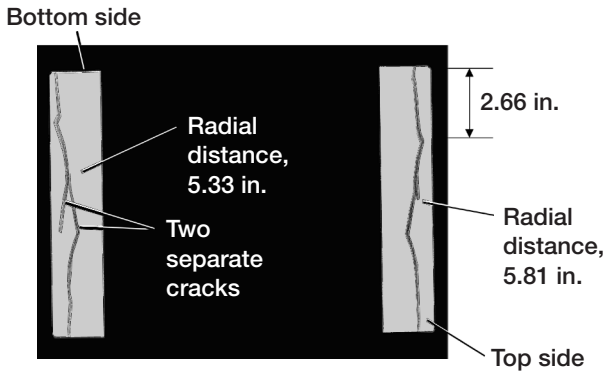

Figure 27.—Cross-sectional computed tomography scan of rotor B showing cracking.

REPORT DOCUMENTATION PAGE

Form Approved
OMB No. 0704-0188

Public reporting burden for this collection of information is estimated to average 1 hour per response, including the time for reviewing instructions, searching existing data sources, gathering and maintaining the data needed, and completing and reviewing the collection of information. Send comments regarding this burden estimate or any other aspect of this collection of information, including suggestions for reducing this burden, to Washington Headquarters Services, Directorate for Information Operations and Reports, 1215 Jefferson Davis Highway, Suite 1204, Arlington, VA 22202-4302, and to the Office of Management and Budget, Paperwork Reduction Project (0704-0188), Washington, DC 20503.

1. AGENCY USE ONLY (*Leave blank*)

2. REPORT DATE
January 2001

3. REPORT TYPE AND DATES COVERED
Technical Memorandum

4. TITLE AND SUBTITLE
Structural Analysis of Composite Flywheels:
An Integrated NDE and FEM Approach

5. FUNDING NUMBERS
WU–494–21–11–00

6. AUTHOR(S)
Ali Abdul-Aziz, George Baaklini, and Jeffrey Trudell

7. PERFORMING ORGANIZATION NAME(S) AND ADDRESS(ES)
National Aeronautics and Space Administration
John H. Glenn Research Center at Lewis Field
Cleveland, Ohio 44135–3191

8. PERFORMING ORGANIZATION REPORT NUMBER
E–12457

9. SPONSORING/MONITORING AGENCY NAME(S) AND ADDRESS(ES)
National Aeronautics and Space Administration
Washington, DC 20546–0001

10. SPONSORING/MONITORING AGENCY REPORT NUMBER
NASA TM—2001-210461

11. SUPPLEMENTARY NOTES
Prepared for the 6th Annual International Symposium on NDE for Health Monitoring and Diagnostics sponsored by The International Society for Optical Engineering, Newport Beach, California, March 4–8, 2001. Responsible person, Ali Abdul-Aziz, organization code 5920, 216–433–6729.

12a. DISTRIBUTION/AVAILABILITY STATEMENT
Unclassified - Unlimited
Subject Category: 24 Distribution: Nonstandard
Available electronically at http://gltrs.grc.nasa.gov/GLTRS
This publication is available from the NASA Center for AeroSpace Information, 301–621–0390.

12b. DISTRIBUTION CODE

13. ABSTRACT ***(Maximum 200 words)***
A structural assessment by integrating finite-element methods (FEM) and a nondestructive evaluation (NDE) of two flywheel rotor assemblies is presented. Composite rotor A is pancakelike with a solid hub design, and composite rotor B is cylindrical with a hollow hub design. Detailed analyses under combined centrifugal and interference-fit loading are performed. Two- and three-dimensional stress analyses and two-dimensional fracture mechanics analyses are conducted. A comparison of the structural analysis results obtained with those extracted via NDE findings is reported. Contact effects due to press-fit conditions are evaluated. Stress results generated from the finite-element analyses were corroborated with the analytical solution. Cracks due to rotational loading up to 48 000 rpm for rotor A and 34 000 rpm for rotor B were successfully imaged with NDE and predicted with FEM and fracture mechanics analyses. A procedure that extends current structural analysis to a life prediction tool is also defined.

14. SUBJECT TERMS
Finite elements; Composite materials; Flywheels; Nondestructive evaluation

15. NUMBER OF PAGES
23

16. PRICE CODE
A03

17. SECURITY CLASSIFICATION OF REPORT	18. SECURITY CLASSIFICATION OF THIS PAGE	19. SECURITY CLASSIFICATION OF ABSTRACT	20. LIMITATION OF ABSTRACT
Unclassified	Unclassified	Unclassified	